Energy & Environmental Science

Accepted Manuscript

ROYAL SOCIETY OF CHEMISTRY

www.rsc.org/ees

As demands for sustainable energy resources are rapidly growing, large scale energy storage technology has recently drawn great interests. Among the energy storage systems, manganese-based electrodes for Na-ion batteries have attracted a great attention for their availability and the low elemental cost of sodium and manganese. However, most of manganese-based electrodes have suffered from the low cycle stability and the poor power capability due to the structural deformation caused by inevitable Jahn-Teller distortion occurring in the presence of Mn^{3+} during battery cycling. For the first time, we report a crystal structure that overcomes this typical problem of manganese-based electrode materials. First-principles calculations reveal that the Jahn-Teller distortion facilitates sodium de/insertion kinetics in this crystal structure by opening up Na diffusion channels. This is the first demonstration of the electrode material that the Jahn-Teller distortion can aid in the electrochemical performance. Our discovery will provide a new insight and a perspective in the development of manganese-based cathode materials for rechargeable batteries.

Journal Name

ARTICLE

Anomalous Jahn-Teller behavior in manganese-based mixed-phosphate cathode for sodium ion batteries

Received 00th January 20xx,
Accepted 00th January 20xx

DOI: 10.1039/x0xx00000x

www.rsc.org/

Hyungsub Kim,[‡ab] Gabin Yoon,[‡ab] Inchul Park,[ab] Kyu-Young Park,[ab] Byungju Lee,[ab] Jongsoon Kim,[ac] Young-Uk Park,[a] Sung-Kyun Jung,[ab] Hee-Dae Lim,[a] Docheon Ahn,[d] Seongsu Lee[c] and Kisuk Kang[ab*]

We report a 3.8-V manganese-based mixed-phosphate cathode material for applications in sodium rechargeable batteries; i.e., $Na_4Mn_3(PO_4)_2(P_2O_7)$. This material exhibits a largest Mn^{2+}/Mn^{3+} redox potential of 3.84 V vs. Na^+/Na yet reported for a manganese-based cathode, together with the largest energy density of 416 Wh kg^{-1}. We describe first-principles calculations and experimental results which show that three-dimensional Na diffusion pathways with low-activation-energy barriers enable the rapid sodium insertion and extraction at various states of charge of the $Na_{4-x}Mn_3(PO_4)_2(P_2O_7)$ electrode (where x = 0, 1, 3). Furthermore, we show that the sodium ion mobility in this crystal structure is not decreased by the structural changes induced by Jahn–Teller distortion (Mn^{3+}), in contrast to most manganese-based electrodes, rather it is increased due to the distortion, which opens up the sodium diffusion channels. This feature stabilizes the material, providing high cycle stability and high power performance for sodium rechargeable batteries. The high voltage, large energy density, cycle stability and the use of low-cost Mn gives $Na_4Mn_3(PO_4)_2(P_2O_7)$ significant potential for applications as a cathode material for large-scale Na-ion batteries.

Introduction

The recent rapid growth in demand for energy has led to increasing interest in sustainable energy resources, such as solar and wind power, in addition to energy generation from conventional fossil fuel resources. An important component in the exploitation of sustainable energy resources is efficient energy storage technology. Large-scale energy storage systems (ESSs) have become an important area of research in recent years.[1, 2] Na-ion batteries (NIBs) are promising candidates for these applications because of the availability and low cost of sodium, as well as the similar electrochemistry to the established Li-ion battery technology.[3-5] However, the low energy density, poor cycle stability and slow sodium kinetics of the existing electrode materials have inhibited the widespread uptake of NIBs.

A number of promising layered sodium-intercalation materials with a high energy density have recently been reported for applications as electrodes in NIBs.[3-5] However, exploitation of sodium in these layered structures with a large number of cycles remains challenging. The large volume change (>10%) during cycling and the phase instability of desodiated structure are among the largest obstacles, and the theoretical capacity remains far from that demonstrated using these layered electrode materials.[6-8] Prussian blue analogues (PBAs) have also been intensively investigated in recent years as promising electrodes for NIBs due to their low element cost, easy synthesis at room temperature and large alkali-ion channel with low activation barriers.[9-11] Although earlier PBAs with a hydrated form showed poor electrochemical activities in Na-ion cells, recent theoretical and experimental studies revealed that the dehydrated PBAs exhibit promising electrochemical properties. The vacuum-dried $Na_2MnFe(CN)_6$ cathode displays superior electrochemical properties compared to other reported PBAs with a hydrated form.[12-13] Polyanion-based compounds have received a wider attention due to its structural stability and the chemical diversity.[14-21] The strong X-O (X = P, S, B, Si) covalent bonding in the structure could offer great structural stability during electrochemical cycling. Furthermore, the rigid open crystal structure is less vulnerable to oxygen evolution at high temperature and exhibits a relatively small volume change associated with sodium-ion insertion/extraction.[14-16] To date, the search for the new polyanion electrodes has focused on iron- and vanadium-based compounds. Iron-based materials, including $Na_2FeP_2O_7$, $Na_2Fe_2(SO_4)_3$, $Na_4Fe_3(PO_4)_2(P_2O_7)$, Na_2FePO_4F, $NaFePO_4$, $NaFeSO_4F$, $Na_2Fe(SO_4)_2{\cdot}2H_2O$, $Na_{4-x}Fe_{2+x/2}(P_2O_7)_2$ and $Na_{2.24}FePO_4CO_3$, are low-cost cathode materials due to the availability of Fe.[14-21] Vanadium-based cathodes include $Na_3V_2(PO_4)_3$, $Na_{1.5}VPO_{5-\delta}F_{0.5+\delta}$, $Na_{1.5}VPO_4F_{1.5}$, $Na_7V_4(P_2O_7)_4PO_4$ and $NaVPO_4F$ are of interest because of the high voltage and

[a] Department of Materials Science and Engineering, Research Institute of Advanced Materials, Seoul National University, 599 Gwanak-ro, Gwanak-gu, Seoul 151-742, Republic of Korea. E-mail: matlgen1@snu.ac.kr
[b] Center for Nanoparticle Research at Institute for Basic Science (IBS), Seoul National University, 599 Gwanak-ro, Gwanak-gu, Seoul 151-742, Republic of Korea
[c] Korea Atomic Energy Research Institute, P.O. Box 105, Daejeon 305-600,Republic of Korea
[d] Beamline Research Division, Pohang Accelerator Laboratory, Pohang 790-784, Republic of Korea

† Electronic Supplementary Information (ESI) available: Detailed structural information of $Na_{4-x}Mn_3(PO_4)_2(P_2O_7)$ ($0 \le x \le 3$) from XRD, ND, XANES and DFT calculation results. See DOI: 10.1039/x0xx00000x

‡ Hyungsub Kim and Gabin yoon contributed equally to this manuscript.

corresponding high energy density.[22-26] There are, however, a number of challenges which must be addressed; these include the low energy density of iron-based cathodes due to the low voltage (typically less than 3.2 V), and the cost issue and environmental impact of vanadium-based compounds.

Along with the iron-based compounds, manganese-based polyanion compounds are attractive alternatives, due to the abundance and ready availability. Recently identified electrode materials include Na_2MnPO_4F, $Na_2MnP_2O_7$ and $Na_3MnPO_4CO_3$, which exhibit electrochemical activity with a higher voltage than is typical for iron-based electrodes.[27-30] While these manganese-based materials have attracted much attention, none have yet been shown to provide sufficiently high performance as electrodes, as they typically suffer from an unacceptably low rate capability and a poor cycle stability. Limited cycle performance of below 30 cycles has been reported.[27-30] Moreover, the large overpotential during charge/discharge even at low current densities has led to a low usable energy density, as well as a low power density. These observations have been made with most manganese-based electrodes, and have been attributed to Jahn–Teller distortion (Mn^{3+}) of the structure during battery cycling. These severe structural distortions lead to deteriorations of the mobility of the ions and of the structural stability, thus rapidly degrading the electrochemical activity of manganese-based cathodes in NIBs.

Here we describe a novel high-voltage mixed-phosphate cathode based on maganese; i.e., $Na_4Mn_3(PO_4)_2(P_2O_7)$, for applications as electrodes in NIBs. This mixed phosphate compound allows fast sodium intercalation kinetics regardless of the state of charges and exhibits a voltage of 3.8 V, which is the highest among known manganese-based NIB cathodes. Furthermore, a reversible capacity of 121 mAh g^{-1} and an energy density of 416 Wh kg^{-1} could be delivered at a rate of C/20 in Na-ion cells, which also represents the largest energy density among manganese-based polyanion NIB cathodes. In addition, our Na-ion cells exhibited stable electrochemical performance over 100 cycles, with 86% retention at a rate of C/5. We attribute this outstanding electrochemical performance to a unique structural feature of our new material where the ionic mobility of sodium is not decreased by the structural changes induced by the Jahn–Teller distortion, rather is actually increased. First principles calculations reveal that this is due to the unique Jahn–Teller distortion of Mn^{3+}, which opens up sodium diffusion channels, enhancing the sodium insertion/extraction kinetics.

Experimental

Synthesis of $Na_4Mn_3(PO_4)_2(P_2O_7)$

$Na_4Mn_3(PO_4)_2(P_2O_7)$ was synthesized *via* a conventional solid-state reaction. A stoichiometric quantity of $Na_4P_2O_7$ (95 %, Aldrich), $Mn_2C_2O_4{\cdot}2H_2O$ (99%, Alfa Aesar) and $NH_4H_2PO_4$ (98% ACS reagent, Aldrich) was mixed using wet ball milling at 200 rpm for 12 hours in acetone. Following ball-milling, the acetone was dried out at 70°C for 12 hours. The mixture was calcinated at 300°C for 6 hours in air, and the resulting powder was pelletized under a pressure of 200 kg cm^{-2}, and sintered again at 600°C for 6 hours in air. Carbon coating of the $Na_4Mn_3(PO_4)_2(P_2O_7)$ sample was carried out to enhance the electrical conductivity using pyromellitic acid (PA) ($C_{10}H_6O_2$, 96%, Alfa Aesar). $Na_4Mn_3(PO_4)_2(P_2O_7)$, and PA were mixed using a planetary ball-milling with a mass ratio of 9:1, and the ground mixture was annealed at 600°C for 2 hours under an Ar atmosphere. The carbon content was approximately 3 wt% of the total powder sample.

Characterization methods

High resolution powder X-ray diffraction (XRD) data of $Na_4Mn_3(PO_4)_2(P_2O_7)$ were obtained from the Beamline 9B at Pohang Accelerator Laboratory (PAL), Republic of Korea. The data were collected over a 2θ range of 10–130°, with a step size of 0.01°, a step time of 7 s and wavelength of $\lambda = 1.54950$ Å. Neutron diffraction (ND) data of $Na_4Mn_3(PO_4)_2(P_2O_7)$ were recorded using a high-resolution powder diffractometer (HRPD) at the HANARO facility in the Korea Atomic Energy Research Institute (KAERI). The measurements were performed over a 2θ range of 0–180° with a step size of 0.05° using a constant wavelength of $\lambda = 1.834333$ Å supplied via a Ge (331) monochromator. The particle size of the samples was examined using field-emission scanning electron microscopy (FESEM) (SUPRA 55VP/Carl Zeiss) and transmission electron microscopy (TEM) (Tecnal F20/FEI). XRD patterns of *ex situ* electrode samples were collected over a 2θ range of 8–60 ° with a step size of 0.02º and step time of 2 s using an X-ray diffractometer (Bruker, D2 PHASER). The valence states and local environment of Mn in the structure of $Na_{4-x}Mn_3(PO_4)_2(P_2O_7)$ ($0 \le x \le 3$) were characterized using X-ray absorption near edge structure (XANES) and X-ray absorption fine structure (EXAFS) analyses. The XANES and EXAFS spectra were obtained from Beamline 7D and 8C at the PAL, Republic of Korea. The Mn k-edge spectra were collected in transmission mode with the electron energy of 2.5 GeV and a current of 200 mA. Mn reference spectra were obtained simultaneously from Mn metal foil.

First-principles calculations

Density functional theory (DFT) calculations were performed to investigate the phase stability, structural evolution during desodiation, and Na diffusion kinetics of $Na_4Mn_3(PO_4)_2(P_2O_7)$. All calculations were carried out using spin-polarized generalized gradient approximation (GGA) parameterized using the Perdew–Burke–Ernzerhof (PBE) exchange model.[31] We further introduced a Hubbard parameter U for Mn, to correct the self-interaction error with the GGA method;[32] we used U_{eff} = 4.5 eV, which were taken from a study on olivine $LiMnPO_4$.[33] Since our study includes both Mn^{2+} and Mn^{3+}, we adopted the average value of U_{eff} from each species. We used projector-augmented wave (PAW) pseudopotentials as implemented in the Vienna *ab initio* simulation package (VASP).[34, 35] After performing the convergence test, a kinetic energy cut-off of 500 eV was used for all calculations, and 1 x 3 x 2 k-point grid was used for geometric relaxations. The structures were relaxed until the remaining force in the unit cell converged within 0.05 eV $Å^{-1}$. We used ferromagnetic ordering of Mn ions because no clear magnetic structure is found by experiments, and our test shows that free energy differences between various magnetic configurations are within a few meVs per formula unit (see Fig. S1).[36]

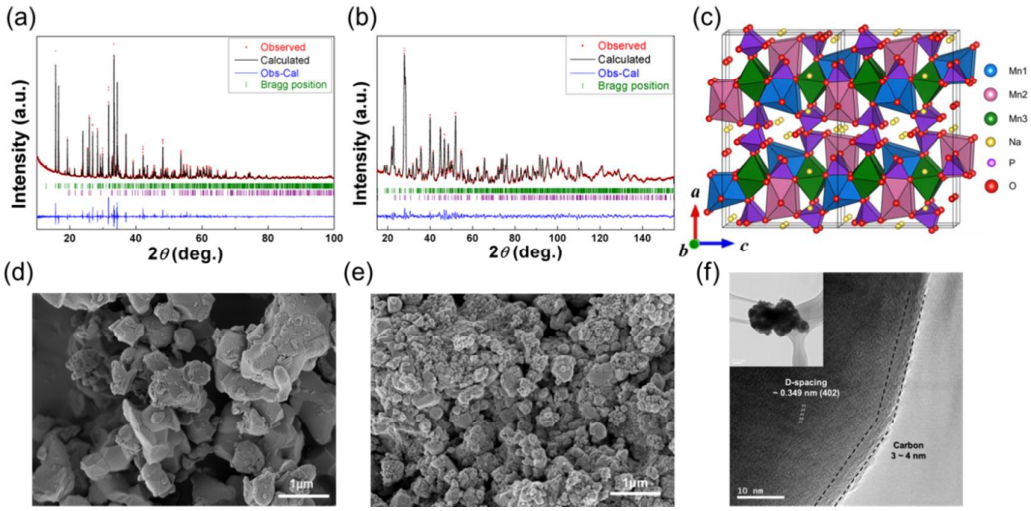

Fig. 1 Rietveld refinement of (a) XRD and (b) ND patterns of $Na_4Mn_3(PO_4)_2(P_2O_7)$. The red symbols illustrate the observed data, the black curves show the calculated patterns, the blue curves show the difference between calculated and observed patterns, and the green symbols show the Bragg position. The $NaMnPO_4$ impurities are shown by the purple markers. (c) Schematic representation of $Na_4Mn_3(PO_4)_2(P_2O_7)$ based on the ND analyses. SEM images of (d) the as-synthesized and (e) carbon-coated $Na_4Mn_3(PO_4)_2(P_2O_7)$. (f) TEM image of the carbon-coated $Na_4Mn_3(PO_4)_2(P_2O_7)$.

To investigate the phase stability and structural evolution, we generated all possible configurations of Na and the vacancies in several Na compositions using four formula units of $Na_{4-x}Mn_3(PO_4)_2(P_2O_7)$ ($0 \leq x \leq 3$) implemented using the CASM software package.[37] Although larger supercells generally yield more accurate results, our unit cell generated more than 16,500 configurations throughout Na compositions, which are large enough to determine the most stable configuration in each Na composition. The 40 lowest electrostatic energy configurations were identified for each composition, as calculated using the Ewald summation method.[38] Further DFT calculations resulted in a convex hull of $Na_{4-x}Mn_3(PO_4)_2(P_2O_7)$ ($0 \leq x \leq 3$), which provided information on the feasible phase reactions and the voltage profiles.

The activation barriers for Na diffusion in the $Na_{4-x}Mn_3(PO_4)_2(P_2O_7)$ (x = 0, 1, 3) structures were determined using the nudged elastic band (NEB) method.[39] A supercell of eight formula units was used to calculate the Na ion diffusion within $Na_{4-x}Mn_3(PO_4)_2(P_2O_7)$ (x = 0, 1, 3). After the initial and final configurations of Na diffusion were determined, five intermediate images were generated *via* linear interpolation of the initial and final images. These were structurally relaxed to provide activation barriers for Na diffusion. The lattice parameters were fixed, whereas all the internal degrees of freedom were allowed to relax.

Electrochemical tests

The electrodes were prepared using $Na_4Mn_3(PO_4)_2(P_2O_7)$, super P and polyvinylidene fluoride (PVDF) with a final mass ratio of 70:20:10. N-methyl-2-pyrrolidone (NMP) (99.5%, Aldrich) was used as a solvent to prepare a slurry of the mixture. The well-mixed slurry was pasted onto Al foil with a 250 μm thickness using a doctor blade, and the NMP was evaporated at 120°C for 1 hour. The loading of $Na_4Mn_3(PO_4)_2(P_2O_7)$ was approximately 2 mg cm^{-2}. The Na half-cell was assembled into a CR2032 coin cell using metallic Na (Sodium cube 99%, Aldrich) as a counter electrode, a glass microfiber filter (grade GF/F; Whatman, US) as a separator. All of the electrochemical tests were carried out by using 1M $NaBF_4$ in EC/PC as an electrolyte which exhibited the most stable electrochemical properties at both room temperature and 60 ºC. The comparison of the electrochemical performances of $Na_4Mn_3(PO_4)_2(P_2O_7)$ electrode in different types of electrolyte such as 1M $NaClO_4$ in EC/PC (1:1 v/v) and 1M $NaPF_6$ in EC/PC (1:1 v/v) can be found in the Fig. S2. Galvanostatic measurements of the charge/discharge of the $Na_4Mn_3(PO_4)_2(P_2O_7)$ electrode were performed with various C-rates (C/20, C/10, C/5, 1C, 2C, 5C, 10C and 20C) at room temperature and at 60°C with cut-off voltages of 1.7 and 4.5 V (*vs.* Na^+/Na). *Ex situ* electrode samples at different states of charge (SOCs) were prepared at a rate of C/20 with a relaxation time of 6 hours to measure the quasi-equilibrium state of the electrodes.

Results and Discussion

Synthesis and characterization of $Na_4Mn_3(PO_4)_2(P_2O_7)$

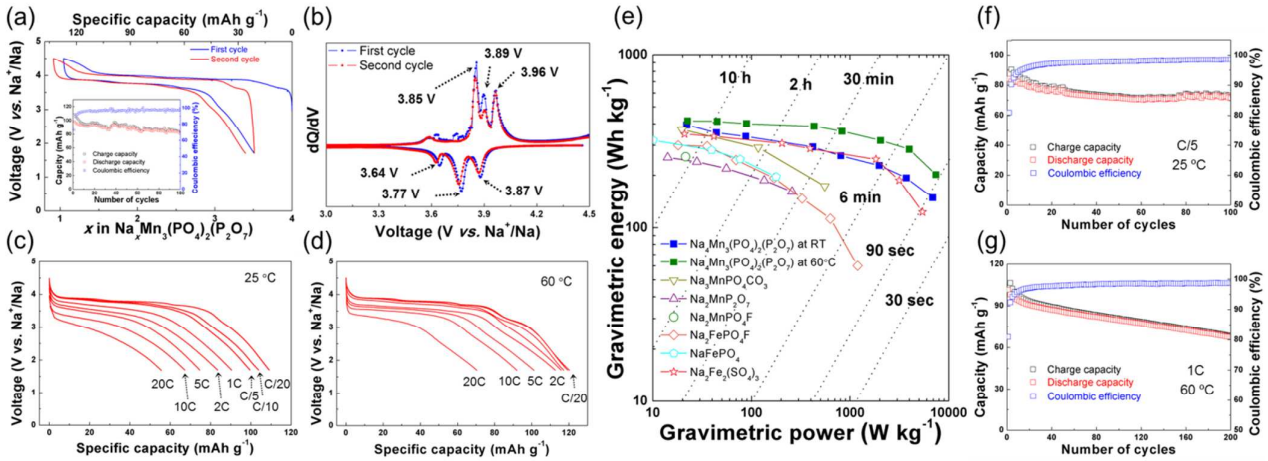

Fig. 2 (a) Charge/discharge profiles of $Na_4Mn_3(PO_4)_2(P_2O_7)$ at a rate of C/20. The first and second cycles are presented by the blue and red curves, respectively. Cycles at a rate of C/20 are shown in the inset. (b) d*Q*/d*V* plots for $Na_4Mn_3(PO_4)_2(P_2O_7)$. The discharge profiles of $Na_4Mn_3(PO_4)_2(P_2O_7)$ at various rates of C/20 to 20C at (c) 25ºC and (d) 60°C. (e) A Ragone plot of $Na_4Mn_3(PO_4)_2(P_2O_7)$ and other representative Fe- and Mn-based polyanion cathode materials for NIBs.[15, 27, 28, 30, 45, 46] The cycle performance of Na-ion cells at (f) C/5 and 25ºC, and (g) 1C and 60°C.

$Na_4Mn_3(PO_4)_2(P_2O_7)$ was successfully synthesized *via* a solid-state reaction at 600°C in air. The crystal structure of the $Na_4Mn_3(PO_4)_2(P_2O_7)$ was investigated using synchrotron X-ray sources, as shown in Fig. 1a. The crystal structure was determined to be orthorhombic $Pn2_1a$, with the following lattice parameters: a = 18.02651 (7) Å, b = 6.65673 (2) Å and c = 10.76886 (4) Å, with a unit volume of 1292.237 (8) Å^3 using Rietveld refinement; this is in a good agreement with a previous report of the crystal structure.[36] The fitting was satisfactory with low reliability factors of R_I = 3.53%, R_F = 2.14%, R_p = 6.84% and R_{wp} = 9.82%. A trace amount of $NaMnPO_4$ (< 4%) was detected. The detailed atomic parameters of $Na_4Mn_3(PO_4)_2(P_2O_7)$ were further investigated using ND analysis, which provides detailed information on the light elements (i.e., Na, P and O), as shown in Fig. 1b. $Na_4Mn_3(PO_4)_2(P_2O_7)$ is isostructural to the existing cathode materials $Na_4Co_3(PO_4)_2(P_2O_7)$ and $Na_4Fe_3(PO_4)_2(P_2O_7)$, but with larger lattice constants, which are attributed to the larger ionic radius of Mn^{2+} (the ionic radius of Mn^{2+} is 0.83 Å, compared with 0.78 Å of Fe^{2+} and 0.745 Å for Co^{2+}).[16, 36, 40, 41] Fig. 1c shows a schematic diagram of the structure of $Na_4Mn_3(PO_4)_2(P_2O_7)$ based on the refinement results of the XRD and ND analyses. The structure is composed of the infinite chains of $[Mn_3P_2O_{13}]_\infty$ blocks along the *bc*-plane, and these blocks are connected along the *a*-axis *via* diphosphate (P_2O_7) groups, which provides the 3D open structure.[16, 36] Three crystallographically distinguishable Mn octahedra sites were identified in the crystal, and these octahedra were connected *via* edge or corner sharing. Detailed structural information, including the atomic parameters and bond valances determined from Rietveld refinement, are listed in Table S1.

The morphology of the $Na_4Mn_3(PO_4)_2(P_2O_7)$ powder was analyzed using scanning electron microscopy (SEM) and transmission electron microscopy (TEM). Fig. 1d shows an SEM image, which indicates that the primary particle size of the as-prepared $Na_4Mn_3(PO_4)_2(P_2O_7)$ power was 0.5–1 µm. Following annealing during the carbon coating process, the particle size reduced to 200–500 nm, due to the ball-milling process with PA, as shown in Fig. 1e. The TEM image shown in Fig. 1f reveals that the carbon was coated onto the surface of the $Na_4Mn_3(PO_4)_2(P_2O_7)$ particles.

Electrochemical properties of $Na_4Mn_3(PO_4)_2(P_2O_7)$

Galvanostatic charge/discharge tests of the $Na_4Mn_3(PO_4)_2(P_2O_7)$ electrodes were carried out at room temperature using Na-ion cells, as shown in Fig. 2a. Almost 100% of the theoretical capacity (i.e., one electron per Mn atom, giving 129.55 mAh g^{-1}) was obtained during the first charge, and 85% of the charge capacity (109 mAh g^{-1}) was delivered during continued discharge at a rate of C/20. Subsequent charge and discharge cycles revealed that the electrochemical reaction of the $Na_4Mn_3(PO_4)_2(P_2O_7)$ electrode was highly reversible, without a notable change in the electrochemical profile. Stable cycle performance was observed, with 82% capacity retention after 100 cycles. Note that the average voltage of the Mn^{2+}/Mn^{3+} redox couple in $Na_{4-x}Mn_3(PO_4)_2(P_2O_7)$ ($0 \le x \le 3$) was 3.84 V. This is the largest Mn^{2+}/Mn^{3+} redox potential (*vs.* Na^+/Na) among Mn-based cathodes yet reported, and comparable to that of the well-known high voltage olivine $LiMnPO_4$ (*vs.* Li^+/Li).[27-30, 42] We believe that the high voltage exhibited by the $Na_4Mn_3(PO_4)_2(P_2O_7)$ electrode is partly due to the Mn octahedra surrounded by the electron-drawing P_2O_7 groups, which have a strong inductive effect.[14, 20, 25, 29, 40, 43] In addition, the edge-sharing geometry of the Mn1-O_6 and Mn3-O_6 polyhedra is expected to lead to a strong Mn^{3+}–Mn^{3+} repulsion in the desodiated structure, which destabilizes the charged state of the electrode, leading to an increased voltage.[15, 43, 44] The average voltage of 3.84 V is clearly shown in the d*Q*/d*V* curves shown in Fig. 2b; three anodic peaks at 3.96, 3.89 and 3.85 V can be clearly distinguished, in addition to the cathodic peaks at 3.87, 3.77, 3.64 V. The multiple peaks in the d*Q*/d*V* profiles imply complex reactions during electrochemical cycling; this will be discussed in detail later in the paper.

We find that the $Na_4Mn_3(PO_4)_2(P_2O_7)$ electrode was capable of reversibly delivering a discharge capacity that was close to

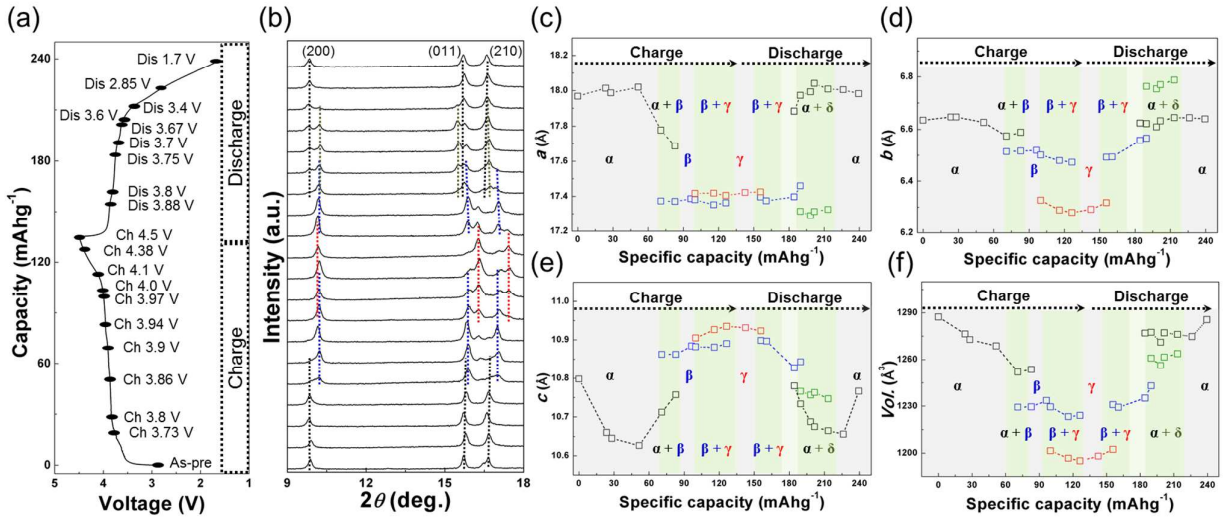

Fig. 3 (a) Galvanostatic charge/discharge profiles of $Na_4Mn_3(PO_4)_2(P_2O_7)$ at a rate of C/20. (b) *Ex situ* XRD patterns of $Na_4Mn_3(PO_4)_2(P_2O_7)$ electrodes during charge/discharge in a Na-ion cell. Changes in the (c) *a*, (d) *b*, (e) *c* lattice parameters and (f) the lattice volume following charging and discharging. The black, blue, red and green markers represent the α, β, γ and δ phases of $Na_{4-x}Mn_3(PO_4)_2(P_2O_7)$ ($0 \le x \le 3$), respectively.

theoretical limit when the kinetic limitations were alleviated. At an elevated temperature of 60°C, a capacity of 121 mAh g^{-1} (i.e., 93% of theoretical capacity) could be delivered at a rate of C/20. This corresponds to an energy density of the $Na_4Mn_3(PO_4)_2(P_2O_7)$ electrode of 416 Wh kg^{-1}, which is the largest of manganese-based NIB cathodes. Note that the energy density of 385 Wh kg^{-1} at 25°C also exceeds that of previously reported manganese-based polyanion cathodes.[27-30] Battery tests at higher current rates show that the $Na_4Mn_3(PO_4)_2(P_2O_7)$ electrode retained significant rate capability both at room temperature and 60°C. Figs. 2c and 2d show discharge profiles of $Na_4Mn_3(PO_4)_2(P_2O_7)$ at rates of C/20, C/10, C/5, 1C, 2C, 5C, 10C and 20C at 25°C and 60°C. A capacity of approximately 112 mAh g^{-1} was delivered at a rate of 2C at 60°C, and 90 mAh g^{-1} was achieved at a rate of 1C at room temperature. More than a half of the theoretical capacity was retained at rates of up to 10C, both at room temperature and 60°C. The Ragone plot shown in Fig. 2e shows the energy and power density of $Na_4Mn_3(PO_4)_2(P_2O_7)$ under various conditions, which is also shown compared with other representative manganese-based polyanion cathodes, as well as recently reported iron-based cathodes for NIBs.[15, 27, 28, 30, 45, 46] It is remarkable that $Na_4Mn_3(PO_4)_2(P_2O_7)$ exhibited the largest gravimetric energy and power densities among these compounds, and these metrics are comparable to those of electrode materials for Li-ion batteries. Moreover, this electrochemical performance was obtained from $Na_4Mn_3(PO_4)_2(P_2O_7)$ with relatively large particles (i.e., 2–500 nm in diameter).

Promising cycle performance was obtained at a rate of C/5 with the cycle retention of 86% and a Coulombic efficiency of 98.5% following 100 cycles, as shown in Fig. 2f. Such capacity retention is unprecedented among manganese-based polyanion compounds, which typically suffer from significant structural distortion due to the presence of Jahn–Teller active Mn^{3+}. Operation at 60°C also exhibited stable retention of 70% at a rate of 1C following 200 cycles, with a Coulombic efficiency of 98.5%, as shown in Fig. 2g. This cycle stability is markedly superior to that of typical manganese-based cathodes at the elevated temperatures, which exhibit rapid capacity decay due to accelerated Mn dissolution.[47]

Structural evolution of the $Na_{4-x}Mn_3(PO_4)_2(P_2O_7)$ electrode during cycling ($0 \le x \le 3$).

To understand the electrochemical activity of $Na_4Mn_3(PO_4)_2(P_2O_7)$ in the Na cell, *ex situ* XRD analysis of the electrodes was performed at different SOCs. Figs. 3a and 3b show *ex situ* XRD patterns of the electrodes during intermediate charge/discharge states. Several multi-phase reactions appeared during cycling, which is consistent with the d*Q*/d*V* data shown in Fig. 2b, which is in marked contrast to the isostructural $Na_4Fe_3(PO_4)_2(P_2O_7)$ electrode, where a single phase electrode reaction occurs throughout the entire charge/discharge process.[48] Nevertheless, slight shifts of the (200), (011) and (210) peaks were observed following charging up to 3.86 V, which is indicative of solid solution behavior of $Na_{4-x}Mn_3(PO_4)_2(P_2O_7)$ (α-phase) during the initial charging process. The *a*- and *b*-lattice constants exhibited negligible change in this solid-solution region, as shown in Figs. 3c and 3d, whereas the *c* lattice parameter and the cell volume decreased continuously, as shown in Figs. 3e and 3f. Following charging to 3.9V, which corresponds to the extraction of approximately 1.64 Na ion, the *a* and *c* lattice parameters underwent relatively large changes, and new peaks appeared in the XRD patterns. This is indicative of the evolution of a new phase (β) in the α-phase matrix. The α-phase fully transformed to β-phase at the Na composition of 2.24 in $Na_{4-x}Mn_3(PO_4)_2(P_2O_7)$, and Rietveld refinement of this β-phase reveals that *a* and *c* lattice parameters differed significantly to those of the α-phase. We speculate that the large lattice mismatch between the α- and β-phases is the cause of the significant distortion of the *a* and *c* lattice parameters of the α-phase during this stage, as well as the apparent phase separation. During charging above 4 V, an additional Na-poor phase (γ-phase) was detected. The new γ-phase exhibited comparable *a* and *c* lattice parameters to those of the β-phase, which in an interesting contrast

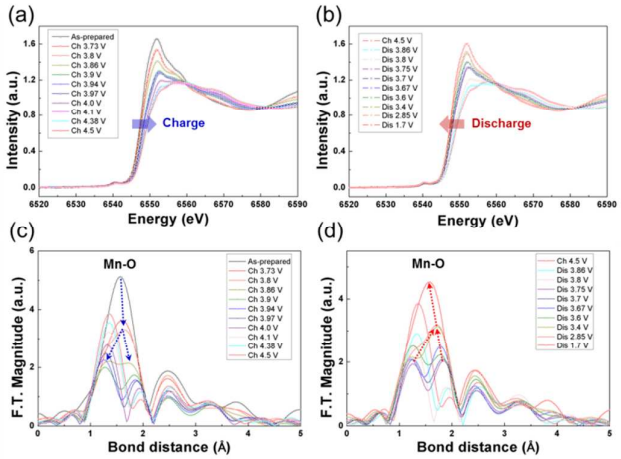

Fig. 4 The XANES spectra of *ex situ* electrode samples of $Na_{4-x}Mn_3(PO_4)_2(P_2O_7)$ ($0 \le x \le 3$) during (a) charge and (b) discharge. The EXAFS spectra of *ex situ* electrode samples of $Na_{4-x}Mn_3(PO_4)_2(P_2O_7)$ ($0 \le x \le 3$) during (c) charge and (d) discharge.

to the case of the phase transition from α to β. Fig. S3c shows the results of Rietveld refinement of the fully charged state (γ-phase). It indicates that after complete charging, the electrode experiences volume contraction of about 7% (compared to the pristine state). This is larger than that of the isostructural $Na_4Fe_3(PO_4)_2(P_2O_7)$ electrode (~4%);[48] however, it should be noted that this volume change following full charging is one of the lowest among manganese-based electrodes (e.g., O3-$NaNi_{0.5}Mn_{0.5}O_2$ exhibits a volume change of 18%, P2-$Na_xFe_{0.5}Mn_{0.5}O_2$ of 11% and olivine $LiMnPO_4$ of 10%).[6, 8, 42] Whereas a large volume change is typically observed for most manganese-based electrodes, due to the occurrence of the significant Mn^{3+} Jahn–Teller distortion during charging, the small volume change of $Na_{4-x}Mn_3(PO_4)_2(P_2O_7)$ is attributed to the unique local environment of Mn in the structure, which will be discussed in more detail in the following section. The *ex situ* XRD patterns of subsequent discharge exhibit a reversible structural evolution from the γ-phase to the α-phase *via* the occurrence of an intermediate β-phase, indicating a reversible electrode reaction. However, a δ-phase also appeared as an additional intermediate phase between β-phase and α–phase. It is uncertain as to the origin of this δ-phase during discharge; however, we speculate that it may arise from specific Na-vacancy ordering, which occurs preferentially in the structure.[18, 25] Detailed structural investigations of this particular composition is part of our ongoing work. Nevertheless, the XRD patterns of the fully discharged electrode were completely restored to its initial as-prepared state, as shown in Fig. S3d. Furthermore, the evolution of XRD patterns during the subsequent charge/discharge cycle was identical to that in the first cycle, as shown in Fig. S4.

Local structural analyses of $Na_{4-x}Mn_3(PO_4)_2(P_2O_7)$ ($0 \le x \le 3$) using *ex situ* XAS

The structural evolution during electrochemical cycling was further analyzed using XAS to monitor the oxidation state and local environment of Mn. Fig. 4a shows XANES spectra of the $Na_{4-x}Mn_3(PO_4)_2(P_2O_7)$ ($0 \le x \le 3$) electrodes during the initial charge process. The clear rightward shift of the XANES spectrum is indicative of oxidation from Mn^{2+} to Mn^{3+}. In addition, the XANES profile gradually altered, showing an isosbestic point at 6559 eV, which is commonly observed in electrode materials that operate *via* a two-phase reaction.[49, 50] The XANES spectrum shifted back to the initial valence state during the discharge process, and the form of the profile also returned to the initial state, as shown in Fig. 4b; this indicates that the electrochemical reaction of $Na_{4-x}Mn_3(PO_4)_2(P_2O_7)$ was reversible in the region of $0 \le x \le 3$. EXAFS analyses also provide information on the local environment of Mn during electrochemical cycling. Fig. 4c shows Fourier transformed (FT) EXAFS spectra of the electrode during charging. The peak corresponding to Mn-O bonds at 1.56 Å exhibited a gradual increase during the initial charging step, and split into two. This suggests the occurrence of Jahn–Teller active Mn^{3+} (indicated by the blue arrow in the figure) in the distorted MnO_6 octahedron, with two long Mn-O bonds and four short Mn-O bonds.[50] The length of the long Mn-O bond was found to be 1.72 Å, whereas that of the short Mn-O bond was 1.35 Å. The FT-EXFAS signals during subsequent discharging to 1.7 V exhibited a completely reversible behavior, as shown in the red arrow in Fig. 4d. The XANES and EXAFS spectra during second charge/discharge cycle were found to be identical to those of the first cycle, as shown in Fig. S5.

Table 1. Desodiation sequence and Mn oxidation states upon charging of $Na_{4-x}Mn_3(PO_4)_2(P_2O_7)$ ($0 \le x \le 3$) based on the DFT calculations.

Sites	Occupancy				Valence state		
	Na1	Na2	Na3	Na4	Mn1	Mn2	Mn3
$Na_4Mn_3(PO_4)_2(P_2O_7)$	1	1	1	1	2+	2+	2+
$Na_{3.5}Mn_3(PO_4)_2(P_2O_7)$	1	0.5	1	1	2+	2+	2+/3+
$Na_3Mn_3(PO_4)_2(P_2O_7)$	1	0	1	1	2+	2+	3+
$NaMn_3(PO_4)_2(P_2O_7)$	0.25	0	0.25	0.5	3+	3+	3+

DFT study on $Na_{4-x}Mn_3(PO_4)_2(P_2O_7)$ ($0 \le x \le 3$)

DFT calculations were carried out to gain insight into the phase reaction of $Na_4Mn_3(PO_4)_2(P_2O_7)$ following desodiation. Fig. 5a shows the formation energy of $Na_{4-x}Mn_3(PO_4)_2(P_2O_7)$ at a few important sodium contents of x ($0 \le x \le 3$). This energy diagram predicts that $Na_4Mn_3(PO_4)_2(P_2O_7)$ undergoes a single-phase reaction until one Na is extracted from the structure, and further Na extraction leads to a two-phase reaction. This behavior corresponds well with our experimental observations (see Figs. 3c–f); however, differs in that a single two-phase reaction is predicted to occur between the α and γ-phases. The absence of a β-phase in the calculations may imply that the β-phase is a kinetically driven intermediate phase between the α- and γ-phases, which is structurally similar to both the α- and γ-phases, even though its origin is not clearly understood. The change in the lattice parameters during desodiation also matches well with the experimental observations, as shown in Fig. 5b. We find negligible changes in the *a* and *b* lattice parameters (< 1%) within the initial solid–solution reaction, and a larger decrease in *c* lattice parameter is shown. Following the extraction of one sodium ion, further charging induces the γ-phase, which has significantly smaller *a* and *b* lattice

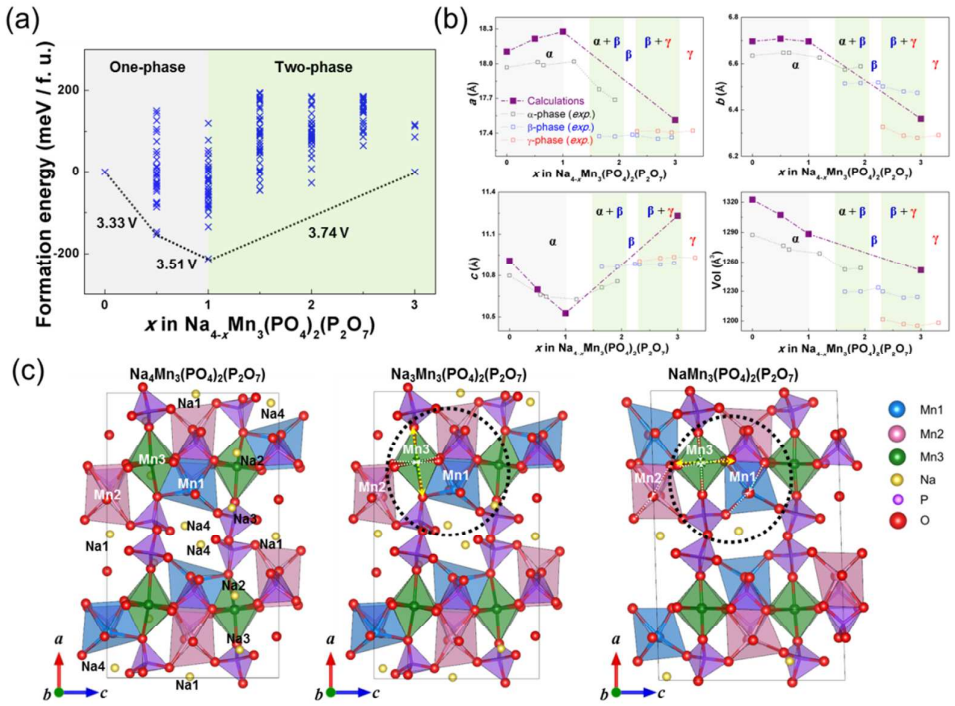

Fig. 5 (a) Formation energy plot of $Na_{4-x}Mn_3(PO_4)_2(P_2O_7)$ ($0 \le x \le 3$). (b) Lattice parameters of each phase in $Na_{4-x}Mn_3(PO_4)_2(P_2O_7)$ ($0 \le x \le 3$), both from the DFT calculations and the experiments. (c) Calculated structures of (left) $Na_4Mn_3(PO_4)_2(P_2O_7)$, (centre) $Na_3Mn_3(PO_4)_2(P_2O_7)$ and (right) $NaMn_3(PO_4)_2(P_2O_7)$.

parameters, and a larger *c* lattice parameter than the α-phase, which is also in a good agreement with experimental results.

Pristine $Na_4Mn_3(PO_4)_2(P_2O_7)$ has four crystallographically distinguishable Na sites and three Mn sites, as shown in Fig. 5c. Upon charging, preferential Na extraction was observed among these sites, along with the corresponding oxidation of Mn, as listed in Table 1. Na ions in the Na2 site are preferentially extracted (i.e., removed first), and oxidation of Mn ions in the Mn3 site occurs simultaneously, which was determined from the spin number numerically integrated around the Mn ion, as shown in Fig. S6. The Mn oxidation preference is also confirmed by the Bader charge analysis and partial density of states (pDOS) calculation (See Table S2 and Fig. S7). The selective oxidation of Mn results in Jahn–Teller distortion in the structure, inducing an increase of the *a* lattice parameter and decrease of *b* and *c* lattice parameters. However, because of the origin distorted nature of the Mn3-O_6 octahedron in the pristine $Na_4Mn_3(PO_4)_2(P_2O_7)$, only a small decrease (~0.1 Å) in the bond lengths in the *bc*-plane occurs, accompanied by a slight elongation of bond lengths in the *a*-direction, as shown in Fig. S8. This appears to be reason for such small changes in the *a* and *b* lattice parameters, despite the Jahn–Teller active Mn^{3+} ion.

The fully desodiated phase, $NaMn_3(PO_4)_2(P_2O_7)$, has one quarter of the Na occupancy in the Na1 and Na3 sites, and half of the Na occupancy in the Na4 (see Table 1). All of the Mn ions are in 3+ oxidation states, regardless of their sites, leading to Jahn–Teller distortion of each of the Mn octahedra. Following oxidation to Mn^{3+}, edge-sharing octahedra of Mn1-O_6 and Mn3-O_6 change to corner-sharing (denoted by the circle in Fig. 5c), which is similar to what is observed in $NaFe_3(PO_4)_2(P_2O_7)$.[48] This phenomenon may be attributed to strong repulsion of between Mn^{3+} ions in the $[Mn_3P_2O_{13}]_\infty$ chain. To accommodate this repulsion, the P_2O_7 dimer distorts to adopt the corner-sharing of the Mn1 and Mn3 octahedra, increasing the distance between Mn1 and Mn3 sites from 3.36 Å to 3.66 Å. This distortion results in a shift of the Mn1 along the *c*-direction, increasing the *c* lattice parameter, which is also verified by the comparison of simulated XRD patterns and experimental ones as shown in Fig. S9. Interestingly, the nature of the Jahn–Teller distortion in the Mn3-O_6 octahedra significantly changes at this stage, as shown in Fig. S8. The initial distortion of the Mn3-O_6 octahedra in $Na_3Mn_3(PO_4)_2(P_2O_7)$ contains two long Mn-O bonds in the *a*-direction (Mn3-O11 and Mn3-O14) and four short bonds in the *bc*-plane (indicated by the yellow and white arrows, respectively, in the centre of Fig. S8). However, this changes to the octahedral form with two long Mn-O bonds in the *bc*-plane (Mn3-O1 and Mn3-O4) and four remaining short Mn-O bonds in the *a*-direction and in the *bc*-plane of $NaMn_3(PO_4)_2(P_2O_7)$ (see the right-hand side of Fig. S8). This is primarily due to the concurrent manifestation of Jahn–Teller distortions in the Mn1-O_6 and Mn2-O_6 octahedra of the fully desodiated state. Because the Mn-O bonds in the Mn1-O_6 and Mn2-O_6 octahedra are shortened along *bc*-plane due to the Jahn–Teller distortion, the Mn3-O_6 octahedron stretches along the *bc*-plane, as shown by yellow arrows in Fig. 5c. This results in the elongation of the Mn3-O1 and Mn3-O4 bonds, and the remaining four Mn-O bonds of Mn3-O_6 octahedron are shortened to maintain the energy gain from the Jahn–Teller distortion.[51, 52]

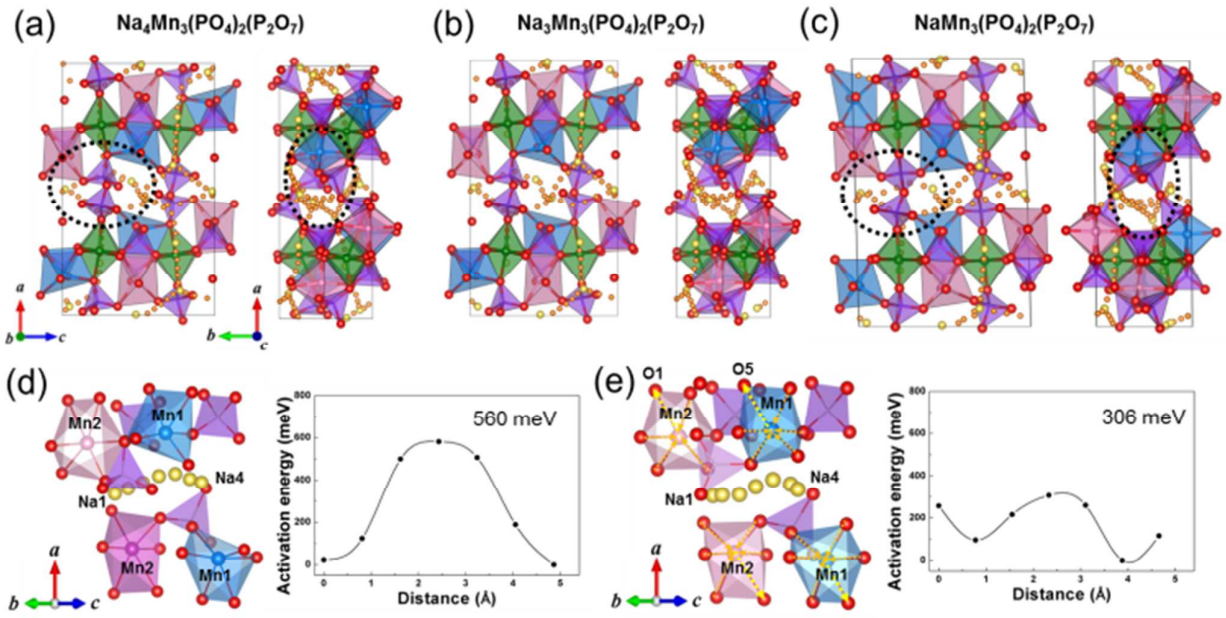

Fig. 6 Na diffusion pathways in (a) $Na_4Mn_3(PO_4)_2(P_2O_7)$, (b) $Na_3Mn_3(PO_4)_2(P_2O_7)$ and (c) $NaMn_3(PO_4)_2(P_2O_7)$. Magnified diffusion pathways of Na ions from the Na1 to Na4 sites (shown by the black circles in (a) and (c)) in (d) $Na_4Mn_3(PO_4)_2(P_2O_7)$ and (e) $NaMn_3(PO_4)_2(P_2O_7)$.

The structural distortion induced by the Jahn–Teller active Mn^{3+} has an important effect on the mobility of Na ions in the structure. Figs. 6a–c show the Na diffusion pathways in the $Na_{4-x}Mn_3(PO_4)_2(P_2O_7)$ (x = 0, 1, 3) structures. A 3D network of interconnected Na diffusion pathways can be clearly seen. One interesting point to note is that, unlike most reported manganese-based cathode materials, Na diffusion is not significantly retarded by the structural changes induced by the Jahn–Teller distortion.[50, 53] While distortion of the P_2O_7 dimer in $NaMn_3(PO_4)_2(P_2O_7)$ causes atomic rearrangements of Mn, P and O ions in the structure (see Fig. S10), according to our calculations of the various Na diffusion pathways, the activation barriers for Na hopping do not increase after the local distortion (see Table 2). It is worthwhile to note that $Na_4Fe_3(PO_4)_2(P_2O_7)$, which shows similar structural evolution to $Na_4Mn_3(PO_4)_2(P_2O_7)$, exhibits slow Na kinetics at this state of charge because of the P_2O_7 distortion and atomic rearrangement which narrows the Na diffusion channels.[48] In the case of $Na_4Fe_3(PO_4)_2(P_2O_7)$, the activation barriers in most Na diffusion paths increase after Fe oxidation as shown in Table S3. After Fe oxidation, there are only limited plausible Na diffusion pathways remaining for $NaFe_3(PO_4)_2(P_2O_7)$, as activation barriers of Na1 – Na4, Na2 – Na4, Na3 – Na2, Na3 – Na4 paths become higher than 500 eV. In particular, as the Na3 – Na2 path closes down due to significantly higher barrier, the 3-dimensional diffusion channel of $Na_4Fe_3(PO_4)_2(P_2O_7)$ does not remain intact (See Fig. S11). In case of $NaMn_3(PO_4)_2(P_2O_7)$, on the contrary, activation barriers of most pathways considerably decrease and 3-dimensional connection of Na diffusion pathways is maintained due to the anomalous behavior of Mn ion distortion.

In order to understand why the activation barriers of most Na diffusion pathways decrease in $Na_4Mn_3(PO_4)_2(P_2O_7)$, we took a closer look at Na1 – Na4 diffusion pathway (denoted by the circle in Figs. 6a and c). We found that Jahn-Teller distortion of Mn1-O_6 and Mn2-O_6 octahedra in $NaMn_3(PO_4)_2(P_2O_7)$ induces a shift of each site in the c-direction; however, the Mn1-O5 and Mn2-O1 bind length increases in the c-direction due to the Jahn–Teller distortion, opening up an Na diffusion channel; i.e., the Na1 – Na4 channel (see Table 2), as shown in Figs. 6 and S8. Closer inspection of the local environment for diffusion between Na1 and Na4 sites indicates that, in the intermediate states of Na diffusion, the distance between the diffusing Na ions and the 6 adjacent O ions, which forms the tunnel space, increases due to the oxidation of Mn1 and Mn2 (see Table S4).

Table 2. The calculated activation barriers for Na diffusion in $Na_{4-x}Mn_3(PO_4)_2(P_2O_7)$. ($x$ = 0, 1, 3)

From (Na site)	To (Na site)	E_a, (meV) $x = 4$	E_a, (meV) $x = 3$	E_a, (meV) $x = 1$
1	1	306	168	282
1	4	560	242	306
2	4	492	>1000	>1000
3	1	209	238	674
3	2	246	243	98
3	4	499	583	288
4	4	271	432	147

The volume of Na-O_6 octahedra in the intermediate state increases from 14.20 $Å^3$ to 15.70 $Å^3$. Accordingly, the activation barrier drastically decreases from 560 meV to 306 meV. This is in clear contrast to the case for Na diffusion in $NaFe_3(PO_4)_2(P_2O_7)$, where the channel narrows significantly due to the shift of Fe1 sites in a-direction and distortion of P_2O_7, which critically increases the activation barrier from 599 meV to 922 meV. (See Table S4 and Fig. S12). Considering that the ionic mobility depends critically on the

space of the diffusion pathways, it is reasonable to expect that the activation barrier for Na ions in the Na1 – Na4 pathway is smaller with $NaMn_3(PO_4)_2(P_2O_7)$, despite the stronger repulsive interaction between Mn^{3+} in the charged state.[54, 55] This unique structural evolution can explain the high rate capability and cycle stability of $Na_4Mn_3(PO_4)_2(P_2O_7)$ observed from the experiments. It is also consistent with the observation that the polarization remains small at the final state of charge in galvanostatic intermittent titration technique (GITT) profiles of $Na_4Mn_3(PO_4)_2(P_2O_7)$, whereas a dramatic increase of overpotential is observed in $Na_4Fe_3(PO_4)_2(P_2O_7)$ (see Fig. S13). Furthermore, this provides an important example structure whereby the Jahn–Teller distortion facilitates Na diffusion that than retarding, it has been reported for most Mn-based cathode materials.[27-30, 50, 53]

Conclusions

We have described a 3.8-V Mn-based mixed-phosphate; i.e., $Na_4Mn_3(PO_4)_2(P_2O_7)$, which was successfully synthesized, and promising electrochemical activity was characterized for the first time. The Mn^{2+}/Mn^{3+} redox potential of 3.84 V *vs.* Na^+/Na is the largest yet reported among manganese-based cathode materials, resulting in a significant increase in the energy density compared with existing materials, representing the largest value yet reported (i.e., 416 Wh kg^{-1}). The high power capability and cycle stability of a manganese-based cathode was observed in Na-ion cells, and is attributed to the unique Jahn–Teller distortion that occurs in this material, which opens up Na diffusion channels, as shown by first principles DFT calculations. The multi-phase reaction with a small lattice volume change of approximately 7% during the electrochemical cycling was found, which also enables the remarkable cycle stability of this material. We believe that the low-cost, stable cycle performances, and high energy density makes $Na_4Mn_3(PO_4)_2(P_2O_7)$ a particularly promising material for cathodes in large-scale Na rechargeable batteries.

Author contributions

Hyungsub Kim, Kyu-Young. Park, Jongsoon Kim, Young-Uk Park, Sung-Kyun Jung and Hee-Dae Lim carried out the synthesis and electrochemical analyses. Gabin Yoon, Inchul Park and Byungju Lee conducted the DFT calculations. Hyungsub Kim, Docheon Ahn and Seoungsu Lee analyzed the crystal structures using neutron and X-ray diffraction patterns. Hyungsub Kim, Gabin Yoon and Kisuk Kang wrote the manuscript. All authors discussed the experiments and contributed to writing the manuscript. Kisuk Kang supervised the research.

Acknowledgements

This work was supported by Project Code (IBS-R006-G1) and the World Premier Materials grant funded by the Korea government Ministry of Trade, Industry and Energy. This work was also supported by National Research Foundation of Korea (NRF) Grant funded by the Korean Government (MSIP) (No. 2014M2B2A4031968, 2012M2A2A6002461 and NRF-2012-Global Ph.D. Fellowship Program). The calculation resources were supported by the Supercomputing Center in Korea Institute of Science and Technology Information (KSC-2012-C2-087).

References

1 J. M. Tarascon and M. Armand, *Nature*, 2001, **414**, 359-367.
2 M. Armand and J. M. Tarascon, *Nature*, 2008, **451**, 652-657.
3 S.-W. Kim, D.-H. Seo, X. Ma, G. Ceder and K. Kang, *Adv. Energy Mater.*, 2012, **2**, 710-721.
4 H. Pan, Y.-S. Hu and L. Chen, *Energy Environ. Sci.*, 2013, **6**, 2338-2360.
5 N. Yabuuchi, K. Kubota, M. Dahbi and S. Komaba, *Chem. Rev.*, 2014, **114**, 11636-11682.
6 N. Yabuuchi, M. Kajiyama, J. Iwatate, H. Nishikawa, S. Hitomi, R. Okuyama, R. Usui, Y. Yamada and S. Komaba, *Nat. Mater.*, 2012, **11**, 512-517.
7 R. Berthelot, D. Carlier and C. Delmas, *Nat. Mater.*, 2011, **10**, 74-80.
8 S. Komaba, N. Yabuuchi, T. Nakayama, A. Ogata, T. Ishikawa and I. Nakai, *Inorg. Chem.*, 2012, **51**, 6211-6220.
9 Y. Lu, L. Wang, J. Cheng and J. B. Goodenough, *Chem. Commun.* 2012, **48**, 6544-6546.
10 L. Wang, Y. Lu, J. Liu, M. Xu, J. Cheng, D. Zhang and J. B. Goodenough, *Angew. Chem. Int. Ed.* 2013, **52,** 1964-1967.
11 Y. You, X. –L. Wu, Y. –X. Yin and Y. –G. Guo, *Energy Environ. Sci.* 2014, **7**, 1643-1647.
12 J. Song, L. Wang, Y. Lu, J. Liu, B. Guo, P. Xiao, J. –J. Lee, X. –Q. Yang, G. Henkelman and J. B. Goodenough, *J. Am. Chem. Soc.* 2015, **137**, 2658-2664.
13 P. Xiao, J. Song, L. Wang, J. B. Goodenough and G. Henkelman, *Chem. Mater.* 2015, **27**, 3763.
14 P. Barpanda, T. Ye, S.-i. Nishimura, S.-C. Chung, Y. Yamada, M. Okubo, H. Zhou and A. Yamada, *Electrochem. Commun.*, 2012, **24**, 116-119.
15 P. Barpanda, G. Oyama, S.-i. Nishimura, S.-C. Chung and A. Yamada, *Nat. Commun.*, 2014, **5**, 4358.
16 H. Kim, I. Park, D.-H. Seo, S. Lee, S.-W. Kim, W. J. Kwon, Y.-U. Park, C. S. Kim, S. Jeon and K. Kang, *J. Am. Chem. Soc.*, 2012, **134**, 10369-10372.
17 B. L. Ellis, W. R. M. Makahnouk, Y. Makimura, K. Toghill and L. F. Nazar, *Nat. Mater.*, 2007, **6**, 749-753.
18 K. T. Lee, T. N. Ramesh, F. Nan, G. Botton and L. F. Nazar, *Chem. Mater.*, 2011, **23**, 3593-3600.
19 P. Barpanda, G. Oyama, C. D. Ling and A. Yamada, *Chem. Mater.*, 2014, **26**, 1297-1299.
20 K.-H. Ha, S. H. Woo, D. Mok, N.-S. Choi, Y. Park, S. M. Oh, Y. Kim, J. Kim, J. Lee, L. F. Nazar and K. T. Lee, *Adv. Energy Mater.*, 2013, **3**, 689-689.
21 W. Huang, J. Zhou, B. Li, J. Ma, S. Tao, D. Xia, W. Chu and Z. Wu, *Sci. Rep.*, 2014, **4**, 4188.
22 Z. Jian, W. Han, X. Lu, H. Yang, Y.-S. Hu, J. Zhou, Z. Zhou, J. Li, W. Chen, D. Chen and L. Chen, *Adv. Energy Mater.*, 2013, **3**, 156-160.
23 Y.-U. Park, D.-H. Seo, H.-S. Kwon, B. Kim, J. Kim, H. Kim, I. Kim, H.-I. Yoo and K. Kang, *J. Am. Chem. Soc.*, 2013, **135**, 13870-13878.
24 R. A. Shakoor, D.-H. Seo, H. Kim, Y.-U. Park, J. Kim, S.-W. Kim, H. Gwon, S. Lee and K. Kang, *J. Mater. Chem.*, 2012, **22**, 20535-20541.
25 S. Y. Lim, H. Kim, J. Chung, J. H. Lee, B. G. Kim, J.-J. Choi, K. Y. Chung, W. Cho, S.-J. Kim, W. A. Goddard, Y. Jung

and J. W. Choi, *Proc. Nat. Acad. Sci. U. S. A.*, 2013, **A111**, 599-604.
26 H. Zhuo, X. Wang, A. Tang, Z. Liu, S. Gamboa and P. J. Sebastian, *J. Power Sources*, 2006, **160**, 698-703.
27 S.-W. Kim, D.-H. Seo, H. Kim, K.-Y. Park and K. Kang, *Phys. Chem. Chem. Phys.*, 2012, **14**, 3299-3303.
28 C. S. Park, H. Kim, R. A. Shakoor, E. Yang, S. Y. Lim, R. Kahraman, Y. Jung and J. W. Choi, *J. Am. Chem. Soc.*, 2013, **135**, 2787-2792.
29 P. Barpanda, T. Ye, M. Avdeev, S.-C. Chung and A. Yamada, *J. Mater. Chem. A*, 2013, **1**, 4194-4197.
30 H. Chen, Q. Hao, O. Zivkovic, G. Hautier, L.-S. Du, Y. Tang, Y.-Y. Hu, X. Ma, C. P. Grey and G. Ceder, *Chem. Mater.*, 2013, **25**, 2777-2786.
31 J. P. Perdew, K. Burke and M. Ernzerhof, *Phys. Rev. Lett.*, 1996, **77**, 3865-3868.
32 V. I. Anisimov, J. Zaanen and O. K. Andersen, *Phys. Rev. B*, 1991, **44**, 943-954.
33 F. Zhou, M. Cococcioni, C. A. Marianetti, D. Morgan and G. Ceder, *Phys. Rev. B*, 2004, **70**, 235121.
34 P. E. Blöchl, *Phys. Rev. B*, 1994, **50**, 17953-17979.
35 G. Kresse and J. Furthmüller, *Comput. Mater. Sci.*, 1996, **6**, 15-50.
36 F. Sanz, C. Parada, J. M. Rojo and C. Ruíz-Valero, *Chem. Mater.*, 2001, **13**, 1334-1340.
37 A. Van der Ven, J. C. Thomas, Q. Xu and J. Bhattacharya, *Math. Comput. Simulat.*, 2010, **80**, 1393-1410.
38 A. Y. Toukmaji and J. A. Board Jr, *Comput. Phys. Commun.*, 1996, **95**, 73-92.
39 G. Henkelman, B. P. Uberuaga and H. Jónsson, *J. Chem. Phys.*, 2000, **113**, 9901-9904.
40 M. Nose, H. Nakayama, K. Nobuhara, H. Yamaguchi, S. Nakanishi and H. Iba, *J. Power Sources*, 2013, **234**, 175-179.
41 R. Shannon, *Acta Crystallogr. Sect. A*, 1976, **32**, 751-767.
42 G. Li, H. Azuma and M. Tohda *Electrochem. Solid-State Lett.*, 2002, **5**, A135-A137.
43 S.-i. Nishimura, M. Nakamura, R. Natsui and A. Yamada, *J. Am. Chem. Soc.*, 2010, **132**, 13596-13597.
44 P. Barpanda, M. Ati, B. C. Melot, G. Rousse, J. N. Chotard, M. L. Doublet, M. T. Sougrati, S. A. Corr, J. C. Jumas and J. M. Tarascon, *Nat. Mater.*, 2011, **10**, 772-779.
45 A. Langrock, Y. Xu, Y. Liu, S. Ehrman, A. Manivannan and C. Wang, *J. Power Sources*, 2013, **223**, 62-67.
46 S.-M. Oh, S.-T. Myung, J. Hassoun, B. Scrosati and Y.-K. Sun, *Electrochem. Commun.*, 2012, **22**, 149-152.
47 Y. Xia, Y. Zhou and M. Yoshio, *J. Elctrochem. Soc.*, 1997, **144**, 2593-2600.
48 H. Kim, I. Park, S. Lee, H. Kim, K.-Y. Park, Y.-U. Park, H. Kim, J. Kim, H.-D. Lim, W.-S. Yoon and K. Kang, *Chem. Mater.*, 2013, **25**, 3614-3622.
49 Y. Orikasa, T. Maeda, Y. Koyama, H. Murayama, K. Fukuda, H. Tanida, H. Arai, E. Matsubara, Y. Uchimoto and Z. Ogumi, *Chem. Mater.*, 2013, **25**, 1032-1039.
50 L. F. J. Piper, N. F. Quackenbush, S. Sallis, D. O. Scanlon, G. W. Watson, K. W. Nam, X. Q. Yang, K. E. Smith, F. Omenya, N. A. Chernova and M. S. Whittingham, *J. Phys. Chem. C*, 2013, **117**, 10383-10396.
51 I. B. Bersuker, *Chem. Rev.*, 2013, **113**, 1351-1390.
52 H. A. Jahn and E. Teller *Proc. R. Soc. A.*, 1937, **161**, 220.
53 B. Xu and S. Meng, *J. Power Sources*, 2010, **195**, 4971-4976.
54 K. Kang and G. Ceder, *Phys. Rev. B*, 2006, **74**, 094105.
55 J. Lee, A. Urban, X. Li, D. Su, G. Hautier and G. Ceder, *Science*, 2014, **343**, 519-522.